PHYSICAL REVIEW B **109**, 155113 (2024)

Spin correlations in the bilayer Hubbard model with perpendicular electric field

Jiawei Yan [*] and Philipp Werner [†]
Department of Physics, University of Fribourg, 1700 Fribourg, Switzerland

(Received 27 December 2023; revised 11 March 2024; accepted 13 March 2024; published 3 April 2024)

We present a nonequilibrium steady-state implementation of the two-particle self-consistent method. This approach respects the Mermin-Wagner theorem and incorporates nonlocal spatial fluctuations through self-consistent static vertices. The real-frequency implementation allows one to compute spectral properties without analytical continuation in both equilibrium and nonequilibrium. As an interesting application, we investigate spin correlations in the bilayer square lattice Hubbard model under a perpendicular static electric field. In equilibrium, the result yields spin correlations which are in good agreement with recent optical lattice experiments. Under a large enough static electric field, the interlayer spin correlations switch from antiferromagnetic to ferromagnetic. We clarify how this phenomenon is linked to the nonequilibrium modifications of the spin excitation spectrum.

DOI: 10.1103/PhysRevB.109.155113

I. INTRODUCTION

The Hubbard model is a minimal model for the description of electron correlation effects in solids. Despite its simplicity, the model exhibits rich equilibrium phase diagrams, which include magnetic phases, charge density waves, and unconventional superconducting states [1,2]. Recent advances in experimental techniques have extended the studies of correlated electron properties to the nonequilibrium domain. An interesting question in this context is the response of correlated electron systems to external electric fields [3,4]. Unfortunately, due to the exponentially growing complexity with system size, the Hubbard model cannot be exactly solved in dimensions $D > 1$, even in the single-band case. The study of electric field effects introduces additional challenges, and necessitates the development of methods capable of addressing nonequilibrium conditions.

For equilibrium studies, powerful computational methods have been devised and used to reveal various Hubbard model properties [5–8]. Dynamical mean-field theory (DMFT) [9,10] distinguishes itself by its nonperturbative nature, which makes it suitable for the study of strong correlation effects and Mott physics. Here, the lattice problem is mapped onto a single impurity coupled to a self-consistently computed noninteracting environment [11,12]. The effective impurity problem can be solved using numerically exact methods, such as quantum Monte Carlo [13,14] or the numerical renormalization group [15,16]. The local nature of the DMFT approximation however makes it unreliable in dimensions $D < 3$, where nonlocal spatial fluctuations become significant. Although cluster or diagrammatic extensions of DMFT partially overcome this limitation, this comes at a considerable computational and storage cost [17,18]. Nonequilibrium calculations have so far been limited to the dynamical cluster approximation (DCA) with small clusters [19–21]. Also, there is an unsolved conceptual issue of how to properly incorporate electric fields into the DCA formalism. Consequently, there is an ongoing quest for novel methods to tackle nonequilibrium Hubbard systems.

Various semianalytical methods capturing spatial correlations have been developed over the past decades [22–26]. These methods rely on renormalized perturbation theory [27,28] and aim to describe correlation effects and critical behaviors by self-consistently calculating irreducible two-particle vertices. This bottom-up approach allows them to mitigate spurious phase transitions that often occur in many-body perturbation theory (MBPT) and DMFT, when applied to low-dimensional systems. In contrast to the dynamical vertex approximation [29] or dual fermion approach [30], these methods assume spatially local and frequency-independent irreducible vertices. These vertices are then determined self-consistently using either the reduced Parquet equation [22–24] or local sum rules [25,26]. The former approach focuses on the qualitatively correct treatment across the entire parameter regime, while the latter aims to predict quantitatively accurate solutions in the weak-to-intermediate correlation regime (up to the regime where local moments emerge in the system) [25]. In this paper, we concentrate on the latter approach, specifically the two-particle self-consistent (TPSC) method, which is extended here to electric field driven nonequilibrium steady states (NESSs).

The TPSC method, originally introduced in Ref. [31], successfully reproduces the pseudogap associated with antiferromagnetic (AFM) spin correlations in the square lattice Hubbard model. The method is formulated in the thermodynamic limit and respects the Mermin-Wagner theorem, Pauli's exclusion principle, particle conservation laws, and various sum rules [25,26]. While originally designed for the single-band Hubbard model, the method has been extended in several directions, to take into account nearest-neighbor interactions [32], spin-orbital couplings [33], and multiorbital interactions [34–36]. Improved TPSC variants, named TPSC+ [37] or TPSC+GG [7], which (partially) feed back the spectral Green's function into the response function calculation, have

---

[*] jiawei.yan@unifr.ch

[†] philipp.werner@unifr.ch

also been developed. A recent addition is the combination of TPSC with DMFT, referred to as TPSC+DMFT, where the TPSC local self-energy is replaced by the DMFT self-energy [38–40]. While these variants violate some sum rules, they enable a deeper exploration of the renormalized classical regime and (in the case of TPSC+DMFT) provide access to the Mott insulating regime. They also alleviate the overestimation of the spin correlations that occurs in the original theory, although this comes at the cost of smoothing out some features of the single-particle spectrum. Moreover, TPSC and related methods are suitable for nonequilibrium extensions, since the underlying approximation on the irreducible vertex (completely local in time and space) significantly simplifies the implementation. Recently, the Anderson impurity model under external bias was studied using reduced Parquet equations [41], and a time-dependent TPSC formalism [with approximate solution of the Bethe-Salpeter equations (BSEs)] was implemented and applied to interaction quenches [40,42].

In this paper, we demonstrate steady-state nonequilibrium extensions of the original TPSC method and of TPSC+GG. In contrast to the time-dependent implementation [40,42], the Bethe-Salpeter equation can be exactly solved in frequency space, which ensures that the sum rules are strictly respected in our steady-state calculations. The real-frequency implementation also avoids the large memory cost for storing two-time Green's functions, and it provides direct access to both equilibrium and nonequilibrium spectral properties without the need for numerical analytical continuation or (windowed) Fourier transformations. As an application, we investigate a bilayer stack of the square lattice Hubbard model under a static perpendicular electric field. Bilayer systems have been the focus of various recent studies, since the manipulation of bonding and antibonding states near the Fermi surface can lead to intriguing phenomena such as pairing correlations in the incipient bands [43,44] and excitonic condensation [45]. Notably, the response to a perpendicular electric field in the bilayer system is nontrivial, in contrast to the single-layer case, which predominantly exhibits a heating effect. In the present paper, we are primarily interested in the spin and charge correlation functions and their responses to the interlayer voltage bias.

The rest of this paper is structured as follows. In Sec. II, we present the theoretical framework. Formally exact many-body equations are introduced in Sec. II A, followed by the TPSC approximation and formalism in Sec. II B. The implementation of our steady-state formalism is detailed in Sec. II C. In Sec. III, the method is applied to the bilayer single-orbital Hubbard model. We introduce the model and setup in Sec. III A and present the equilibrium and nonequilibrium results in Secs. III B and III C, respectively. In Sec. IV, we give a brief conclusion, while detailed derivations and some TPSC+GG results are provided in the Appendixes.

II. THEORY

We consider a single-band Hubbard model described by the Hamiltonian

$$\mathcal{H}(t) = \sum_{ij}\sum_{\sigma} W_{ij}(t)c^{\dagger}_{i\sigma}c_{j\sigma} + \sum_{i} U_i(t)\hat{n}_{i\uparrow}\hat{n}_{i\downarrow}. \tag{1}$$

Here, $c^{(\dagger)}_{i\sigma}$ represents the annihilation (creation) operator for site i with spin σ, and $\hat{n}_{i\sigma} = c^{\dagger}_{i\sigma}c_{i\sigma}$ denotes the corresponding density operator. The on-site interaction is denoted by U_i and the hopping amplitude from site j to site i is denoted by W_{ij}. The chemical potential has been absorbed into the on-site components of the hopping matrix W.

A. Many-body theory

We start with formally exact equations from MBPT. A central quantity in this theory is the single-particle Green's function G, which is defined as

$$G_{\sigma}(1,2) = -i\langle T_{\gamma}c_{\sigma}(1)c^{\dagger}_{\sigma}(2)\rangle, \tag{2}$$

where we adopt a compressed notation $1 \equiv (i,z)$, with i and z referring to the site and contour time, and σ denoting spin. T_{γ} is the time ordering operator on the contour γ, which, in the most general case, runs from t_0 to some maximum time $t_{\max}$ along the real axis, back to zero along the real axis, and then to $-i\beta$ (with $\beta = 1/T$ the inverse temperature) along the imaginary-time axis [46]. (In the steady-state implementation, we employ a two-branch Schwinger-Keldysh contour [47].) T_{γ} orders the operators from right to left with increasing contour time, with an additional minus sign for the exchange of two fermionic operators. $\langle\cdots\rangle = \frac{1}{Z}\mathrm{Tr}[e^{-i\int_{\gamma}d\bar{z}\mathcal{H}(\bar{z})}\cdots]$ denotes the expectation value, with $Z = \mathrm{Tr}[e^{-i\int_{\gamma}d\bar{z}\mathcal{H}(\bar{z})}]$ the partition function of the initial equilibrium state. Physically, $G_{\sigma}(1,2)$ represents the probability amplitudes for a single particle propagating in the interacting system.

By taking the derivative of Eq. (2) with respect to time z and considering the commutation relations of the operators, one obtains the equation of motion (EOM) of $G_{\sigma}(1,2)$, which in the case of the Hubbard model, Eq. (1), can be expressed as

$$\sum_{k}\left[\delta_{ik}i\frac{d}{dz} - W_{ik}(z)\right]G_{kj,\sigma}(z,z')$$
$$= \delta_{ij}\delta(z-z') - iU_i(z)\langle T_{\gamma}\{\hat{n}_{i-\sigma}(z)c_{i\sigma}(z), c^{\dagger}_{j\sigma}(z')\}\rangle. \tag{3}$$

The second term on the right-hand side of this equation results from the Coulomb interactions. We define the interaction self-energy Σ_{σ}, which encodes how interactions affect the propagation of the electrons, through

$$[\Sigma_{\sigma} * G_{\sigma}](1,2) = -iU(1)\langle T_{\gamma}\{\hat{n}_{-\sigma}(1)c_{\sigma}(1), c^{\dagger}_{\sigma}(2)\}\rangle. \tag{4}$$

By introducing the noninteracting Green's function

$$\sum_{k}\left[\delta_{ik}i\frac{d}{dz} - W_{ik}(z)\right]G^{0}_{kj,\sigma}(z,z') = \delta_{ij}\delta(z-z'), \tag{5}$$

one arrives at the Dyson equation

$$G_{\sigma}(1,2) = G^{0}_{\sigma}(1,2) + \left[G^{0}_{\sigma} * \Sigma_{\sigma} * G_{\sigma}\right](1,2). \tag{6}$$

Here, we use the short-hand notation $[A*B](1,2) = \int_{\gamma} d\bar{3}A(1,\bar{3})B(\bar{3},2)$ to denote convolutions over both the space and time domains. Equation (3) connects single-particle quantities (left-hand side) to two-particle quantities (right-hand side), and shows that in an interacting system two-particle correlations affect the single-particle dynamics.

To quantify this, we introduce the generic four-point susceptibility

$$i\chi_{\sigma\sigma'}(1,2,3,4) = \langle T_\gamma\{c_\sigma(1)c_{\sigma'}(2)c^\dagger_{\sigma'}(4)c^\dagger_\sigma(3)\}\rangle + G_\sigma(1,3)G_{\sigma'}(2,4), \tag{7}$$

which satisfies the BSE

$$\begin{aligned}\chi_{\sigma\sigma'}&(1,2,3,4)\\ &= G_\sigma(1,4)G_{\sigma'}(2,3)\delta_{\sigma\sigma'}\\ &\quad - G_\sigma(1,\bar{1})G_\sigma(\bar{3},3)\Lambda_{\sigma\bar{\sigma}}(\bar{1},\bar{2},\bar{3},\bar{4})\chi_{\bar{\sigma}-\sigma}(\bar{4},2,\bar{2},4),\end{aligned} \tag{8}$$

where $\Lambda_{\sigma\bar{\sigma}}(\bar{1},\bar{2},\bar{3},\bar{4})$ is the irreducible vertex. We use the convention that variables with overbars are integrated over, and in the second term we introduced the compact notation $\chi_{\sigma\sigma'}(1,2,3,4) \equiv \chi_{\sigma\sigma'\sigma\sigma'}(1,2,3,4)$. Appendix A details the derivation of the above equations. Combining Eqs. (3), (7), and (8), we obtain the Schwinger-Dyson equation for the self-energy:

$$\begin{aligned}\Sigma_\sigma(1,2) = &-iU(1)G_{-\sigma}(1,1^+)\delta(1-2) + U(1)G_\sigma(1,\bar{1})\\ &\times \Lambda_{\sigma\bar{\sigma}}(\bar{1},\bar{2},2,\bar{4})\chi_{\bar{\sigma}-\sigma}(\bar{4},1,\bar{2},1^+).\end{aligned} \tag{9}$$

Here, $1^+ \equiv (i, z^+)$, where z^+ is shifted by an infinitesimal time along the contour, relative to z.

In the following, we focus on paramagnetic states, where G_σ becomes spin independent and $\chi_{\sigma\sigma'}$ can be transformed into contributions from spin and charge channels. We define the spin and charge susceptibilities as $\chi^{\mathrm{ch}} = \sum_{\sigma\sigma'}\chi_{\sigma\sigma'}$ and $\chi^{\mathrm{sp}} = \sum_{\sigma\sigma'}\sigma\sigma'\chi_{\sigma\sigma'}$. The physical two-point correlations are given by $\chi^{\mathrm{sp/ch}}(1,2) = \chi^{\mathrm{sp/ch}}(1,2,1^+,2^+)$, which can be expressed as

$$i\chi^{\mathrm{sp}}(1,2) = \langle \mathcal{T}_\gamma\{\hat{S}^z(1),\hat{S}^z(2)\}\rangle, \tag{10a}$$

$$i\chi^{\mathrm{ch}}(1,2) = \langle \mathcal{T}_\gamma\{\hat{N}(1),\hat{N}(2)\}\rangle - N(1)N(2). \tag{10b}$$

Here, consistent with the naming convention, $\hat{N}(1) = \hat{n}_\uparrow(1) + \hat{n}_\downarrow(1)$ and $\hat{S}^z(1) = \hat{n}_\uparrow(1) - \hat{n}_\downarrow(1)$ are the total density and spin-z operators (without factor $1/2$), respectively. If one takes the limit $2 \to 1^+$ in Eq. (10), one obtains the following local spin and charge sum rules [48]:

$$i\chi^{\mathrm{sp}}(1,1^+) = N(1) - 2\langle\hat{n}_\uparrow(1)\hat{n}_\downarrow(1)\rangle, \tag{11a}$$

$$i\chi^{\mathrm{ch}}(1,1^+) = 2\langle\hat{n}_\uparrow(1)\hat{n}_\downarrow(1)\rangle - [N(1)]^2 + N(1), \tag{11b}$$

where we used the property $(\hat{n}_\sigma)^2 = \hat{n}_\sigma$.

B. TPSC method

The central approximation in TPSC is the following Hartree-type decomposition of Eq. (3):

$$\left[\Sigma^{(1)}_\sigma * G^{(1)}_\sigma\right](1,2) = -i\lambda(1)U(1)G^{(1)}_\sigma(1,2)G^{(1)}_{-\sigma}(1,1^+), \tag{12}$$

where $\lambda(1)$ is introduced as a renormalization factor to the bare Coulomb interaction. The superscript "(1)" denotes the Green's function and the self-energy defined in the first-level approximation. The explicit expression of the self-energy can be obtained by multiplying with $(G_\sigma)^{-1}$ from the right:

$$\Sigma^{(1)}_\sigma(1,2) = -i\lambda(1)U(1)G^{(1)}_{-\sigma}(1,1^+)\delta(1-2). \tag{13}$$

If $\lambda(1)$ equals unity, this reduces to the conventional Hartree diagram. The renormalized Coulomb interaction implies that the chemical potential should also be renormalized to give the correct filling.

The thermodynamically consistent irreducible vertex is obtained as $\Lambda_{\sigma\sigma'}(1,2,3,4) = -\delta\Sigma^{(1)}_\sigma(1,3)/\delta G^{(1)}_{\sigma'}(4,2)$ [49], which yields

$$\begin{aligned}\Lambda_{\sigma\sigma'}(1,2,3,4) = iU(1)\delta(1-3)\Bigg[&\lambda(1)\delta_{\sigma'-\sigma}\delta(1-4)\delta(1^+-2)\\ &+ \frac{\delta\lambda(1)}{\delta G^{(1)}_{\sigma'}(4,2)}G^{(1)}_{-\sigma}(1,1^+)\Bigg].\end{aligned} \tag{14}$$

We furthermore assume that the second term in the brackets is proportional to $\delta(1-4)\delta(1^+-2)$, to obtain the following local form of the spin and charge vertices:

$$\Lambda^{\mathrm{sp/ch}}(1,2,3,4) = i\tilde{\Lambda}^{\mathrm{sp/ch}}(1)\delta(1-3)\delta(1-4)\delta(1^+-2), \tag{15}$$

where we defined $\tilde{\Lambda}^{\mathrm{ch/sp}} = \tilde{\Lambda}_{\uparrow\downarrow} \pm \tilde{\Lambda}_{\uparrow\uparrow}$. The factor i in Eq. (15) is a convention which makes $\tilde{\Lambda}(1)$ a real scalar. One can easily see that

$$\tilde{\Lambda}^{\mathrm{sp}}(1) = \lambda(1)U(1), \tag{16}$$

since $\delta\lambda(1)/\delta G^{(1)}_\uparrow = \delta\lambda(1)/\delta G^{(1)}_\downarrow$ in the paramagnetic phase.

Given the completely local form of $\tilde{\Lambda}^{\mathrm{sp/ch}}$, the BSEs can be simplified to

$$\chi^{\mathrm{ch/sp}}(1,2) = \chi^0(1,2) \pm \tfrac{1}{2}\chi^0(1,\bar{1})\tilde{\Lambda}^{\mathrm{ch/sp}}(\bar{1})\chi^{\mathrm{ch/sp}}(\bar{1},2), \tag{17}$$

where χ^0 in Eq. (17) is the bare response function (also known as the Lindhard function) given by

$$\chi^0(1,2) = -2iG^{(1)}(1,2)G^{(1)}(2,1). \tag{18}$$

Provided that the double occupancy is known, the sum rules in Eq. (11) allow one to fix the local vertices $\tilde{\Lambda}^{\mathrm{sp/ch}}$, since $\chi^{\mathrm{sp/ch}}$ depend on $\tilde{\Lambda}^{\mathrm{sp/ch}}$ via the BSEs. This is used for example in the recently developed TPSC+DMFT approach [38].

In the original TPSC, however, a further local field approximation (LFA) is introduced to self-consistently obtain the double occupancy without external input [50]. This is based on the fact that $\langle\hat{n}_\uparrow(1)\hat{n}_\downarrow(1)\rangle$ is spatially local and does not strongly depend on the nearby sites. Specifically, in the hole doped case with density (per spin) $n = N/2$, the LFA makes the approximation

$$\lambda(1) = \frac{\langle\hat{n}^{(1)}_\uparrow(1)\hat{n}^{(1)}_\downarrow(1)\rangle}{n^{(1)}(1)n^{(1)}(1)}, \tag{19}$$

where $\langle\hat{n}^{(1)}_\uparrow(1)\hat{n}^{(1)}_\downarrow(1)\rangle$ denotes the double occupancy in the first-level approximation. In the electron doped case, one should replace $\hat{n}_\sigma$ with $1-\hat{n}_\sigma$ in Eq. (19) [25]. With this approximation, the Hartree decomposition, Eq. (12), becomes identical to the EOM [Eq. (3)] in the limit $2 \to 1^+$.

The self-consistent calculation of the two-particle vertices contains the following steps.

(i) Start with some initial guess for the double occupancy $\langle \hat{n}_\uparrow^{(1)} \hat{n}_\downarrow^{(1)} \rangle$ and calculate the corresponding $\tilde{\Lambda}^{\mathrm{sp}}$ using Eqs. (19) and (16).

(ii) Solve the spin channel BSE (17) to obtain χ^{sp}.

(iii) Update the double occupancy, $\langle \hat{n}_\uparrow^{(1)} \hat{n}_\downarrow^{(1)} \rangle$, using Eq. (11a). Repeat the procedures (i)–(iii) until convergence is reached in the spin channel.

(iv) Once the spin channel is converged, use the converged value of $\langle \hat{n}_\uparrow^{(1)} \hat{n}_\downarrow^{(1)} \rangle$ on the right-hand side of Eq. (11b) and search for the $\tilde{\Lambda}^{\mathrm{ch}}$ which satisfies this sum rule.

The above thermodynamically consistent two-particle self-consistency is also known as the first-level TPSC iteration.

Once the vertices $\tilde{\Lambda}^{\mathrm{sp/ch}}$ and susceptibilities $\chi^{\mathrm{sp/ch}}$ have been obtained in both the spin and charge channels, the spectral self-energy can be obtained by solving the Schwinger-Dyson equation, Eq. (9). Specifically, in the paramagnetic phase with local irreducible vertices, we have

$$\Sigma^{(2)}(1,3) = -iU(1)G^{(1)}(1,1^+)\delta(1-3) + \Sigma^C[\alpha](1,3), \tag{20}$$

where the first term is the usual Hartree contribution and

$$\begin{aligned}\Sigma^C[\alpha](1,3) = \frac{iU(1)}{8}G^{(1)}(1,3)\alpha(3)[\tilde{\Lambda}^{\mathrm{ch}}(3)\chi^{\mathrm{ch}}(3,1)\\ + 3\tilde{\Lambda}^{\mathrm{sp}}(3)\chi^{\mathrm{sp}}(3,1)]\end{aligned} \tag{21}$$

is the correlation self-energy obtained by averaging the longitudinal and transversal channels [51]. In Eq. (20) , the superscript “(2)” denotes the second-level spectral self-energy. The coefficient α in Eq. (21), which renormalizes the vertices, is determined by the local sum rules in the spectral calculation [25,42], i.e., by the condition

$$[\Sigma^{(2)}[\alpha] * G^{(2)}](1,1^+) = iU(1)\langle \hat{n}_\uparrow^{(1)}(1)\hat{n}_\downarrow^{(1)}(1)\rangle. \tag{22}$$

Here, $G^{(2)}$ is the spectral Green’s function corresponding to $\Sigma^{(2)}$. The α renormalization has been found to be important for real-time simulations, possibly due to the approximation introduced in solving the BSEs [42]. However, in the present steady-state implementation, we find that it has almost no effect on the results. We thus keep $\alpha = 1$ in all our calculations.

It is noteworthy that, for a generic system (such as the bilayer lattice out of equilibrium, as discussed later), the iteration of $G^{(1)}(1,2)$ is essential to achieve first-level self-consistency. This is due to the fact that $\Sigma^{(1)}(1,2)$ in Eq. (13) is site dependent and different from a noninteracting system with a shifted chemical potential. Consequently, the Lindhard function [Eq. (18)] and Bethe-Salpeter equations need to be recalculated in each self-consistency loop. If $\Sigma^{(1)}(1,2)$ is site independent (for example in a single band or bilayer system in equilibrium), this self-consistency process can be simplified since the constant shift of the first-level self-energy can be absorbed into the global chemical potential.

Moreover, the original TPSC does not work deep inside the renormalized classical regime, where antiferromagnetic spin fluctuations exponentially increase as the system temperature decreases [25]. To gauge the validity of the results, in addition to comparing with numerically exact methods, one can perform internal accuracy checks by measuring the difference between $\mathrm{Tr}[\Sigma^{(2)} * G^{(1)}]$ and $\mathrm{Tr}[\Sigma^{(2)} * G^{(2)}]$, where the former one can be proven to be equal to $iU\langle \hat{n}_\uparrow^{(1)} \hat{n}_\downarrow^{(1)} \rangle$ [25] (see Appendix B for more details). The relative error is defined by

$$\text{rel. error} = \left| \frac{\mathrm{Tr}[\Sigma^{(2)} * G^{(1)}] - \mathrm{Tr}[\Sigma^{(2)} * G^{(2)}]}{\mathrm{Tr}[\Sigma^{(2)} * G^{(1)}]} \right|. \tag{23}$$

One of the recently developed improved TPSC variants, TPSC+GG, feeds the spectral Green’s function $G^{(2)}$ back to χ^0 in Eq. (18), thus reaching a self-consistency loop [7,40]. Even though this approach in principle violates the local sum rules, numerical tests show an improvement of the two-particle correlation functions, compared to QMC results [7].

C. Steady-state implementation

For the steady-state implementation of the formulas, we adopt a two-branch Schwinger-Keldysh contour, assuming that initial correlations of the system have been wiped out upon relaxation into a time-translation invariant steady state [47]. We further assume the existence of translational invariance in the lattice model. The general procedure for the steady-state implementation involves obtaining the real-time equations by applying Langreth’s rules [46,47] to the equations for the contour γ, followed by Fourier transformation of the relevant components to frequency and momentum space to facilitate the implementation [41,52,53]. This technique allows one to simulate both thermal equilibrium states and nonequilibrium steady states, and to obtain spectral functions without the need for numerical analytical continuation.

We use the vector $\mathbf{B}$ to denote a site within the unit cell and $\mathbf{T}$ to represent the translation vector between unit cells. Thus, a generic site corresponds to the vector $\mathbf{R} = \mathbf{B} + \mathbf{T}$. (In the case of the bilayer lattice considered in Sec. III, the unit cell consists of two sites.) We adopt the Fourier transform convention

$$O_{\mathbf{B}\mathbf{B}'}(\omega;\mathbf{k}) = \sum_{\mathbf{T}} O_{(\mathbf{B}+\mathbf{T})\mathbf{B}'}(t)e^{i(\omega t - \mathbf{k}\cdot\mathbf{T})}, \tag{24a}$$

$$O_{(\mathbf{B}+\mathbf{T})\mathbf{B}'}(t) = \frac{1}{2\pi N_{\mathbf{k}}}\sum_{\mathbf{k}}\int d\omega O_{\mathbf{B}\mathbf{B}'}(\omega;\mathbf{k})e^{-i(\omega t - \mathbf{k}\cdot\mathbf{T})}, \tag{24b}$$

where $N_{\mathbf{k}}$ is the number of $\mathbf{k}$ points (unit cells). For simplicity, we omit the superscripts “(1)” and “(2)” in the following subsection. In frequency-momentum space, the BSE for the spin (charge) channel, Eq. (17), reads

$$\chi_{\mathbf{B}\mathbf{B}'}^{\mathrm{sp(ch)},r/a}(\omega;\mathbf{q}) = \chi_{\mathbf{B}\mathbf{B}'}^{0,r/a}(\omega;\mathbf{q}) \mp \frac{1}{2}\sum_{\bar{\mathbf{B}}}\chi_{\mathbf{B}\bar{\mathbf{B}}}^{0,r/a}(\omega;\mathbf{q})\tilde{\Lambda}_{\bar{\mathbf{B}}}^{\mathrm{sp(ch)}}\chi_{\bar{\mathbf{B}}\mathbf{B}'}^{\mathrm{sp(ch)},r/a}(\omega;\mathbf{q}), \tag{25a}$$

$$\chi_{\mathbf{B}\mathbf{B}'}^{\mathrm{sp(ch)},\lessgtr}(\omega;\mathbf{q}) = \chi_{\mathbf{B}\mathbf{B}'}^{0,\lessgtr}(\omega;\mathbf{q}) \mp \frac{1}{2}\sum_{\bar{\mathbf{B}}}\left[\chi_{\mathbf{B}\bar{\mathbf{B}}}^{0,r}(\omega;\mathbf{q})\tilde{\Lambda}_{\bar{\mathbf{B}}}^{\mathrm{sp(ch)}}\chi_{\bar{\mathbf{B}}\mathbf{B}'}^{\mathrm{sp(ch)},\lessgtr}(\omega;\mathbf{q}) + \chi_{\mathbf{B}\bar{\mathbf{B}}}^{0,\lessgtr}(\omega;\mathbf{q})\tilde{\Lambda}_{\bar{\mathbf{B}}}^{\mathrm{sp(ch)}}\chi_{\bar{\mathbf{B}}\mathbf{B}'}^{\mathrm{sp(ch)},a}(\omega;\mathbf{q})\right], \tag{25b}$$

where the upper minus sign is for the spin channel and the lower plus sign is for the charge channel, and the superscript r (a) refers to the retarded (advanced) components. The Lindhard function (18) becomes

$$\chi^{0,r/a}_{\mathbf{BB'}}(\omega;\mathbf{q}) = -\frac{i}{\pi}\frac{1}{N_{\mathbf{k}}}\sum_{\mathbf{k}}\int_{-\infty}^{\infty} dx\big[G^{r/a}_{\mathbf{BB'}}(x;\mathbf{k}+\mathbf{q})G^{<}_{\mathbf{B'B}}(x-\omega;\mathbf{k}) + G^{<}_{\mathbf{BB'}}(x;\mathbf{k}+\mathbf{q})G^{a/r}_{\mathbf{B'B}}(x-\omega;\mathbf{k})\big], \tag{26a}$$

$$\chi^{0,\lessgtr}_{\mathbf{BB'}}(\omega;\mathbf{q}) = -\frac{i}{\pi}\frac{1}{N_{\mathbf{k}}}\sum_{\mathbf{k}}\int_{-\infty}^{\infty} dx G^{\lessgtr}_{\mathbf{BB'}}(x;\mathbf{k}+\mathbf{q})G^{\gtrless}_{\mathbf{B'B}}(x-\omega;\mathbf{k}). \tag{26b}$$

The local spin and charge sum rules in Eq. (11) can be expressed as

$$\frac{1}{N_{\mathbf{k}}}\sum_{\mathbf{q}}\frac{1}{2\pi}\int_{-\infty}^{\infty} d\omega \chi^{\mathrm{sp},<}_{\mathbf{BB}}(\omega;\mathbf{q}) = -i[N_{\mathbf{B}} - 2\langle\hat{n}_{\mathbf{B}\uparrow}\hat{n}_{\mathbf{B}\downarrow}\rangle], \tag{27a}$$

$$\frac{1}{N_{\mathbf{k}}}\sum_{\mathbf{q}}\frac{1}{2\pi}\int_{-\infty}^{\infty} d\omega \chi^{\mathrm{ch},<}_{\mathbf{BB}}(\omega;\mathbf{q}) = i\big[N_{\mathbf{B}}^2 - N_{\mathbf{B}} - 2\langle\hat{n}_{\mathbf{B}\uparrow}\hat{n}_{\mathbf{B}\downarrow}\rangle\big]. \tag{27b}$$

For the spectral calculation, we use $\Sigma^{r/a}_{\mathbf{BB'}}(\omega;\mathbf{k}) = U_{\mathbf{B}}n_{\mathbf{B}}\delta_{\mathbf{BB'}} + \Sigma^{C,r/a}_{\mathbf{BB'}}(\omega;\mathbf{k})$ and $\Sigma^{\lessgtr}_{\mathbf{BB'}}(\omega;\mathbf{k}) = \Sigma^{C,\lessgtr}_{\mathbf{BB'}}(\omega;\mathbf{k})$, where the self-energy contributions from electron correlations are given by

$$\begin{aligned}\Sigma^{C,r/a}_{\mathbf{BB'}}(\omega;\mathbf{k}) = &+\frac{i}{8N_{\mathbf{k}}}\sum_{\mathbf{q}}\frac{1}{2\pi}\int_{-\infty}^{\infty} dx G^{r/a}_{\mathbf{BB'}}(x;\mathbf{k}+\mathbf{q})\alpha_{\mathbf{B'}}\big[\tilde{\Lambda}^{\mathrm{ch}}_{\mathbf{B'}}\chi^{\mathrm{ch},<}_{\mathbf{B'B}}(x-\omega;\mathbf{q})U_{\mathbf{B}} + 3\tilde{\Lambda}^{\mathrm{sp}}_{\mathbf{B'}}\chi^{\mathrm{sp},<}_{\mathbf{B'B}}(x-\omega;\mathbf{q})U_{\mathbf{B}}\big]\\ &+\frac{i}{8N_{\mathbf{k}}}\sum_{\mathbf{q}}\frac{1}{2\pi}\int_{-\infty}^{\infty} dx G^{<}_{\mathbf{BB'}}(x;\mathbf{k}+\mathbf{q})\alpha_{\mathbf{B'}}\big[\tilde{\Lambda}^{\mathrm{ch}}_{\mathbf{B'}}\chi^{\mathrm{ch},a/r}_{\mathbf{B'B}}(x-\omega;\mathbf{q})U_{\mathbf{B}} + 3\tilde{\Lambda}^{\mathrm{sp}}_{\mathbf{B'}}\chi^{\mathrm{sp},a/r}_{\mathbf{B'B}}(x-\omega;\mathbf{q})U_{\mathbf{B}}\big],\end{aligned} \tag{28a}$$

$$\Sigma^{C,\lessgtr}_{\mathbf{BB'}}(\omega;\mathbf{k}) = \frac{i}{8N_{\mathbf{k}}}\sum_{\mathbf{q}}\frac{1}{2\pi}\int_{-\infty}^{\infty} dx G^{\lessgtr}_{\mathbf{BB'}}(x;\mathbf{k}+\mathbf{q})\alpha_{\mathbf{B'}}\big[\tilde{\Lambda}^{\mathrm{ch}}_{\mathbf{B'}}\chi^{\mathrm{ch},\gtrless}_{\mathbf{B'B}}(x-\omega;\mathbf{q})U_{\mathbf{B}} + 3\tilde{\Lambda}^{\mathrm{sp}}_{\mathbf{B'}}\chi^{\mathrm{sp},\gtrless}_{\mathbf{B'B}}(x-\omega;\mathbf{q})U_{\mathbf{B}}\big]. \tag{28b}$$

Note that we have the symmetry relations $\chi^{r/a}_{\mathbf{BB'}}(\omega;\mathbf{q}) = \chi^{a/r}_{\mathbf{B'B}}(-\omega;-\mathbf{q})$ and $\chi^{\lessgtr}_{\mathbf{BB'}}(\omega;\mathbf{q}) = \chi^{\gtrless}_{\mathbf{B'B}}(-\omega;-\mathbf{q})$ both for χ^0 and $\chi^{\mathrm{sp/ch}}$.

The most time-consuming part in the evaluation of the above formulas is calculating the convolutions in frequency-momentum space, such as $C(\omega;\mathbf{q}) = \frac{1}{2\pi N_{\mathbf{k}}}\sum_{\mathbf{k}}\int_{-\infty}^{\infty} dx A(x;\mathbf{k}+\mathbf{q})B(x-\omega;\mathbf{k})$. In our implementation, we employ fast Fourier transformation to the time-position domain, where the convolutions become pointwise multiplications. As a result, the computational complexity reduces from $N_\omega^2 N_{\mathbf{k}}^2$ to $N_\omega N_{\mathbf{k}} \log(N_\omega N_{\mathbf{k}})$, where N_ω and $N_{\mathbf{k}}$ are the number of frequency and $\mathbf{k}$ points, respectively. Additionally, since our implementation works with real frequencies, and the spectra may contains delta peaks (for example, in the case of the thermodynamic Green's function $G^{(1)}$), a broadening of poles has to be introduced. However, since our model will be coupled to external baths (see below), the smearing of the poles is taken care of by these baths.

As sketched in Fig. 1(a), the model is coupled to external leads, which are assumed to be in local equilibrium with chemical potential μ_α (α = top, bottom) and inverse temperature β. For $\mu_{\mathrm{top}} > \mu_{\mathrm{bottom}}$ the system is in a nonequilibrium steady state with a particle current flowing from the top to the bottom lead [54]. The effect of the leads is described by the lead self-energy, which depends on the detailed lead setup. Here, for simplicity, we adopt the wide-band limit (WBL), which assumes a flat density of states near the Fermi level with half bandwidth D. The explicit expression for the WBL lead self-energy (retarded component) for site i and spin channel σ is

$$\Sigma^{\mathrm{ld},r}_{i\sigma}(\omega) = \frac{\Gamma_{i\sigma}}{\pi}\ln\left|\frac{D+(\omega-\mu_i)}{D-(\omega-\mu_i)}\right| - i\Gamma_{i\sigma}\theta(|\omega-\mu_i| < D), \tag{29}$$

where $\Gamma_{i\sigma}$ is the coupling strength of the $i\sigma$ channel and θ is the Heaviside step function. The lesser part can be obtained from the fluctuation-dissipation theorem,

$$\Sigma^{\mathrm{ld},<}_{i\sigma}(\omega) = -2if_\beta(\omega-\mu_i)\mathrm{Im}\Sigma^{\mathrm{ld},r}_{i\sigma}(\omega), \tag{30}$$

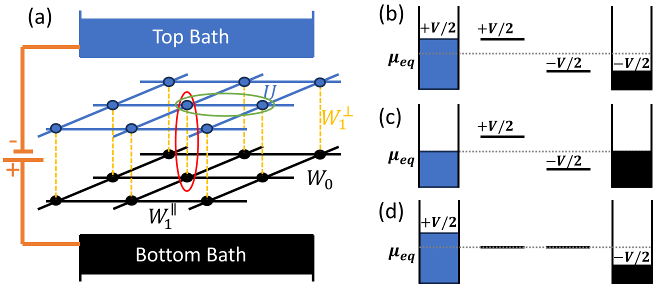

FIG. 1. (a) Schematic illustration of the bilayer square lattice Hubbard model with external voltage bias. Red and green ellipses mark nearest-neighbor inter- and intralayer correlations, respectively. (b)–(d) Real-space self-energy diagram for the model with (b) both local energy and lead chemical potential shifts, (c) only local energy shifts (equilibrium doping model), and (d) only lead chemical potential shifts.

with f_β the Fermi function for inverse temperature β, since the leads are assumed to be in local equilibrium. Note that the lead self-energy is site diagonal in the WBL and that the total lead self-energy is the sum of $\Sigma^{\mathrm{ld}}_{i\sigma}(\omega)$ over sites i. (Generically, the total lead self-energy could contain off-diagonal terms, which make it $\mathbf{k}$ dependent.) As follows from Fig. 1(a), the lead self-energy from the top (bottom) bath is added to the sites in the top (bottom) layer. The red and green ellipses in Fig. 1(a) mark two sites for measuring nearest-neighbor inter- and intralayer correlations, as discussed in the following.

III. NUMERICAL RESULTS

A. Setup

We focus in the main text on a bilayer stack of the square lattice Hubbard model, with each layer coupled to a free-electron bath, as shown in Fig. 1(a). The unit cell of the model comprises two sites, and in the noninteracting case the dispersion relation reads

$$\epsilon_\pm(\mathbf{k}) = 2W_1^{\parallel}[\cos(k_x a) + \cos(k_y a)] \pm W_1^{\perp} + W_0, \qquad (31)$$

where $a = 1$ is the lattice constant, $W_1^{\parallel}$ and $W_1^{\perp}$ are the site-independent inter- and intralayer hoppings, and W_0 is the on-site energy, as depicted in Fig. 1. The plus and minus signs in Eq. (31) refer to bonding (symmetric) and antibonding (antisymmetric) states resulting from the interlayer hopping. One can also introduce a Fourier transform along the stacking direction, in which case the former (latter) state corresponds to $k_\perp = 0$ ($k_\perp = \pi$).

The baths are assumed to have an equilibrium distribution with inverse temperature β. An external applied voltage bias V shifts their local energy levels and chemical potentials and results in a perpendicular electric field across the bilayer structure. In most of the calculations, we assume that the voltage drop occurs only between the top and bottom layers, as depicted in Fig. 1(b). (A more advanced modeling would self-consistently determine the voltage profile by considering the charge density and Hartree potential.) In our simple setup, the voltage bias has two main consequences: (i) a reshuffling of charge between the layers due to the different on-site energies of the two layers and (ii) nonequilibrium distributions in the layers due to the different local chemical potentials in the baths. To distinguish these two effects, we also consider two additional models: (i) a model with only shifted on-site energies of the layers, but identical chemical potentials in the baths (the equilibrium doping model), depicted in Fig. 1(c), and (ii) a model with only shifted chemical potentials in the baths but unchanged local energies in the layers, depicted in Fig. 1(d). Note that the electronic states in the central layers are identical for the configurations in Figs. 1(b) and 1(c). This allows us to examine how nonequilibrium effects alter the system's behavior by changing the populations of the electronic states. In the following nonequilibrium calculations, our default model is the one shown in Fig. 1(b), unless otherwise stated.

In the numerical calculations, we use a grid of 64×64 $\mathbf{k}$ points and 2^{16} frequency points on each side of the real-frequency axis, spaced by $d\omega = 10^{-3}$ to achieve a fine spectral resolution. The computation time for each calculation is approximately 20 minutes when executed with 64 CPU cores.

B. Thermal equilibrium

We first examine the equilibrium properties of the particle-hole symmetric system. The parameters chosen in our paper are $U = 4$ and inverse temperature $\beta = 4$ (unless otherwise stated), and the coupling to each free-electron bath is $\Gamma = 0.05$ (wide-band approximation). We set $W_1^{\parallel} = 1$ as the energy unit.

Figure 2 presents the equilibrium ($\mu_{\mathrm{top}} = \mu_{\mathrm{bottom}}$) single-particle quantities calculated by the original TPSC and for different interlayer hoppings: $W_1^{\perp} = 0$ [Fig. 2(a)], $W_1^{\perp} = 0.25$ [Fig. 2(b)], $W_1^{\perp} = 0.5$ [Fig. 2(c)], and $W_1^{\perp} = 1.0$ [Fig. 2(d)]. From left to right, the three columns in Fig. 2 display (i) the local spectral function $A(\omega)$ and occupation, (ii) the correlated band structure $A(\omega; \mathbf{k})$ along a high symmetry path, $\Gamma = (0, 0) \to X = (\pi, 0) \to M = (\pi, \pi) \to \Gamma = (0, 0)$, and (iii) the "Fermi surface" $A(\omega = 0; \mathbf{k})$. The shaded area in the left panels marks the equilibrium distribution of occupied states, $A(\omega)f_\beta(\omega)$, where $f_\beta(\omega)$ is the Fermi function for inverse temperature β.

In the case $W_1^{\perp} = 0$, the two layers are decoupled and the model reduces to the single-layer square lattice model. The corresponding local spectral function, shown in Fig. 2(a), features a pseudogap at the Fermi energy, indicative of strong antiferromagnetic correlations in the system. Indeed, the band structure and Fermi surface reveal a suppression of spectral weight at the X point, $\mathbf{k} = (\pi, 0)$, which results in a discontinuous Fermi surface. The destruction of quasiparticles near the antinode is consistent with the findings from other advanced many-body methods, such as cluster DMFT or dual fermions [55,56], but the TPSC approach is computationally much cheaper. TPSC+GG results are presented in Appendix C, where it is shown that this modified formalism does not produce an antiferromagnetic pseudogap in the spectral function for the same parameters.

Figures 2(b)–2(d) show how the electronic structure evolves as a function of the interlayer hopping $W_1^{\perp}$. One can see that the pseudogap at the Fermi level persists if $W_1^{\perp}$ is increased. The underlying physics however changes, since the bilayer system exhibits a crossover from a pseudogap induced by antiferromagnetic correlations to a bonding/antibonding-type band splitting, as can be deduced from the band structures and Fermi surfaces [57]. As shown in the right panels, the Fermi surface represented by $A(\omega = 0; \mathbf{k})$ undergoes a nontrivial evolution: starting from a pseudogap pattern with disconnected segments, spectral weight redistribution leads to a splitting into two full Fermi surfaces with increasing $W_1^{\perp}$.

In Fig. 3, we focus on the spin correlations for $W_1^{\perp} = 0$ (equivalent to the single-layer case). Figures 3(a) and 3(b) depict the static spin susceptibility $-\frac{1}{\pi}\mathrm{Im}\chi^{\mathrm{sp},>}(\mathbf{q}; \omega = 0)$ obtained using TPSC and TPSC+GG, respectively. One can see hot spots appearing at the corner $\mathbf{q} = (\pi, \pi)$ of the Brillouin zone, which confirms the existence of antiferromagnetic correlations in the system. These correlations are strong in the TPSC solution, but much weaker in TPSC+GG (note the difference in the color bars), consistent with the

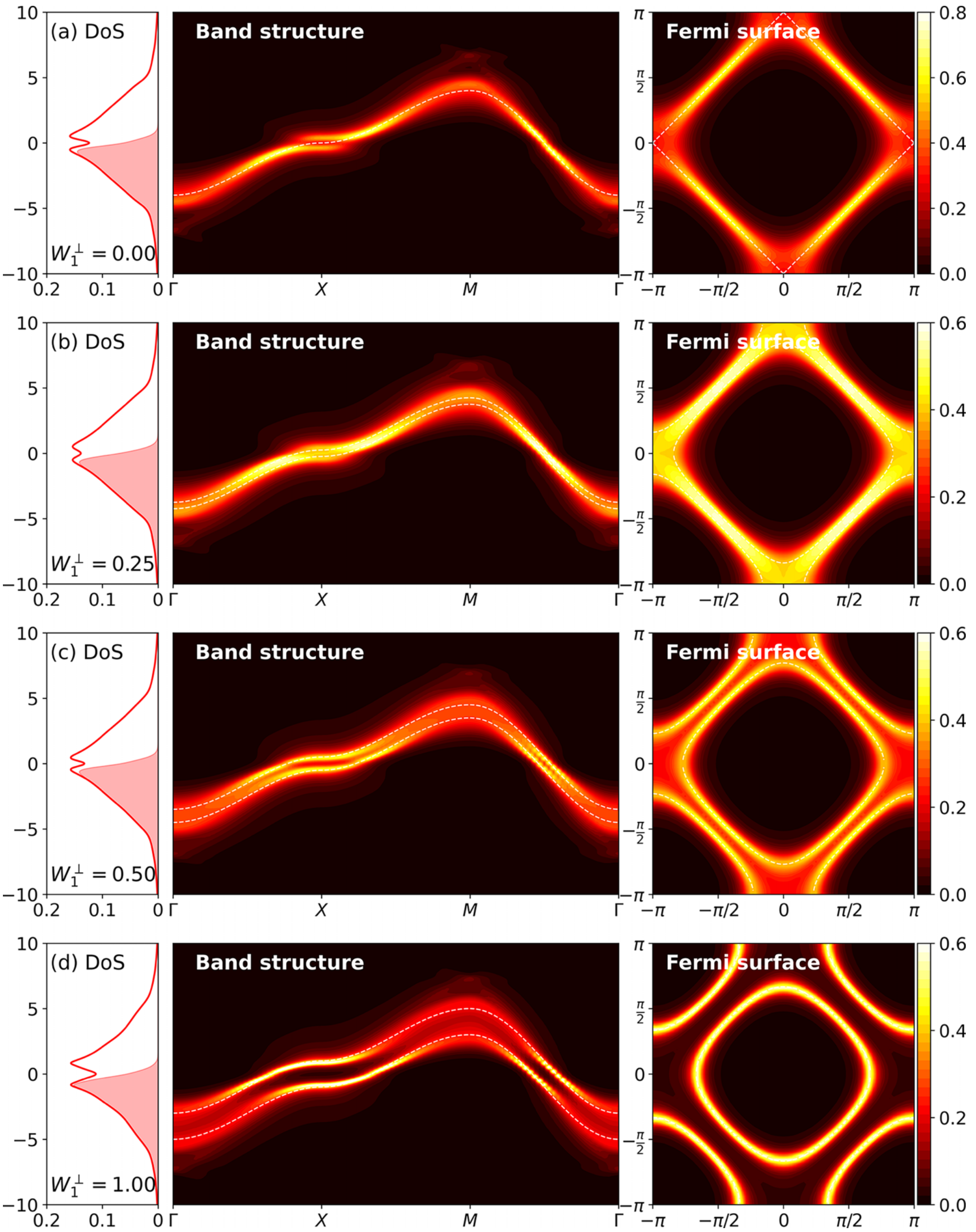

FIG. 2. Local spectral function $A(\omega)$ (shaded area for occupied states), momentum-resolved spectral function $A(\mathbf{k};\omega)$, and "Fermi surface" $A(\omega=0;\mathbf{k})$ of the bilayer square lattice Hubbard model with (a) $W_1^\perp = 0$, (b) $W_1^\perp = 0.25$, (c) $W_1^\perp = 0.5$, and (d) $W_1^\perp = 1.0$. Thin white dashed lines are the noninteracting band structures and Fermi surfaces. (Equilibrium system, $U = 4$, $\beta = 4$.)

presence/absence of a pseudogap in the fermionic spectral function noted above. In Fig. 3(c), we plot the corresponding real-space instantaneous ($t' \to t$) spin-spin correlations obtained by the Fourier transform:

$$\langle \hat{S}^z_{\mathbf{B}} \hat{S}^z_{\mathbf{B}'+\mathbf{T}} \rangle = \frac{i}{2\pi N_{\mathbf{k}}} \sum_{\mathbf{q}} \int_{-\infty}^{\infty} d\omega\, \chi^{\mathrm{sp},>}_{\mathbf{B}\mathbf{B}'}(\omega;\mathbf{q}) e^{-i\mathbf{q}\cdot\mathbf{T}}. \qquad (32)$$

The x axis corresponds to the distance (in units of lattice spacing) from the origin along the x direction. By symmetry, the result is the same along the y direction. Due to the more smeared-out spin excitation spectrum, the TPSC+GG curve exhibits a faster decay compared to the TPSC result, indicating a shorter antiferromagnetic correlation length in the former method.

Previous studies have noted the overestimation of the spin correlation length by TPSC [7,40], and it has been shown that TPSC+GG significantly improves the two-particle correlations. Based on this, one might conclude that the TPSC+GG results with shorter correlation length and nonexistent pseudogap should be more reliable for the present parameters. On the other hand, it has been shown that self-consistent resummations via "boldification" of diagrams can lead to inaccurate results [58] and in particular to unphysical fermionic spectral functions. A well-known example is the boldified second-order perturbation theory, which leads to a strong smearing

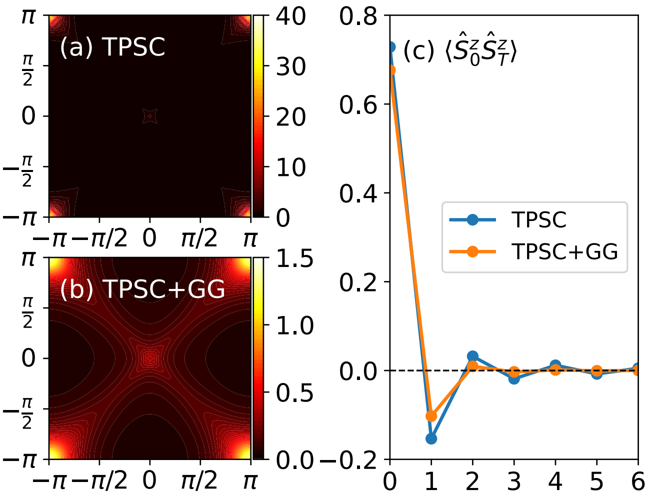

FIG. 3. Momentum-resolved spin correlations $-\frac{1}{\pi}\mathrm{Im}\chi^{\mathrm{sp},>}(\omega = 0;\mathbf{q})$ for the single-layer ($W_1^\perp = 0$) Hubbard model obtained by (a) TPSC and (b) TPSC+GG. Note the different range of the color bars. (c) Corresponding real space spin-spin correlations $\langle \hat{S}^z_0 \hat{S}^z_T \rangle$. The horizontal axis shows the distance (in units of lattice spacing) from the origin along the x direction. (Equilibrium system, $U = 4$, $\beta = 4$.)

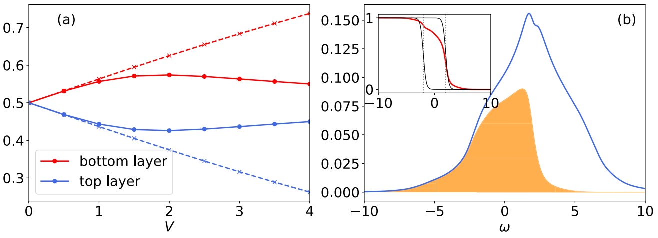

FIG. 5. (a) Electron density in the two layers vs voltage bias V. Solid and dashed lines show the results corresponding to the models in Figs. 1(b) and 1(c), respectively. (b) Spectral function of the top layer (blue line) $A_{\mathrm{top}}(\omega)$ for $V = 4$ and occupied states $A^<(\omega)$ (orange shading). Inset: Corresponding nonequilibrium distribution function $f_{\mathrm{neq}}(\omega)$ (red). The black solid and gray dashed lines show the bath distribution functions and chemical potentials, respectively. (Parameters: $W_1^\perp = 1$, $U = 4$, $\beta = 4$.)

of the spectral function and overdamped nonequilibrium dynamics [10,59].

In the subsequent discussions, we primarily focus on the original TPSC method, which will be used to study the out-of-equilibrium behavior of the bilayer system. Before that, we first benchmark the method using equilibrium data from a recent optical lattice experiment [60]. To ensure consistency with Ref. [60], we adopt the same parameters $U = 8$, $\beta = 1$, and $n = 0.4$ (average filling for each spin channel). In Fig. 4(a), we plot the intralayer spin structure factor $\frac{i}{2\pi}\int \chi^{\mathrm{sp},>}_{00}(\omega;\mathbf{q})d\omega$ as a function of interlayer coupling $W_1^\perp$. Results are shown for $\mathbf{q} = (0, 0)$ (red color) and $\mathbf{q} = (\pi, \pi)$ (blue color). The dots with error bars represent the experimental data extracted from Fig. 2(b) in Ref. [60], where an optical lattice based quantum simulator was employed to study the bilayer Hubbard model. Note that for the purpose of this comparison, the TPSC data are divided by 4, since there is a factor 1/2 difference in the definition of the spin operator in Ref. [60]. The good agreement of the TPSC curves in Fig. 4(a) with the data from the optical lattice experiment provides support for the reliability of our method in the parameter regime considered in this paper. In Fig. 4(b), we show the corresponding inter- and intralayer spin correlations, defined by Eq. (32), in red and blue, respectively. As $W_1^\perp$ increases, the interlayer spin correlations become negative, because the electrons on the different layers tend to form interlayer singlets. Simultaneously, the intralayer nearest-neighbor spin correlations approach zero, since neighboring singlets become independent.

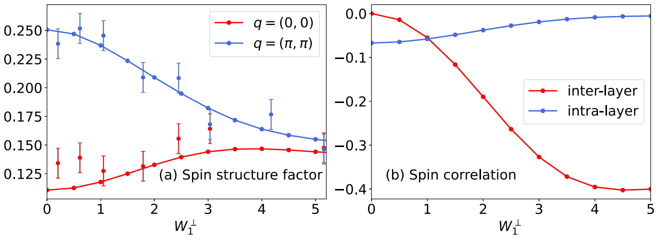

FIG. 4. (a) Intralayer spin structure factor (divided by 4) for $\mathbf{q} = (0, 0)$ and (π, π). The dots with error bars show the experimental data extracted from Ref. [60]. (b) Corresponding nearest-neighbor inter- and intralayer spin-spin correlations defined in Eq. (32). (Equilibrium system, $U = 8$, $\beta = 1$, density per spin $n = 0.4$.)

In all these equilibrium calculations, the internal error, as defined in Eq. (23), remains below 10%. This indicates that the results in the chosen parameter regime do not have any obvious internal inconsistencies.

C. Nonequilibrium steady state

We next apply a voltage bias V across the bilayer system with $U = 4$, to generate a static electric field perpendicular to the layers. More specifically, the on-site energies of the top and bottom layers, as well as the respective baths, are shifted by $\pm V/2$ from their equilibrium values, as illustrated in Fig. 1(b). As a result, electrons start to flow from the top to the bottom layers and the system reaches a steady state (controlled by V and the bath coupling Γ) after a sufficiently long time, which is the regime we analyze in the following.

1. Single-particle properties

We start with the single-particle properties plotted in Fig. 5 for $W_1^\perp = 1$. Figure 5(a) shows how the electron density (red for the bottom layer and blue for the top layer) varies as a function of the voltage bias. Solid lines plot the densities calculated for the nonequilibrium model [Fig. 1(b)], while the dashed lines are the results for the equilibrium model with shifted on-site energies [Fig. 1(c)]. With increasing V, there is a reshuffling of charge from the top to the bottom layer. (We neglect the effect of this reshuffling on the electric field or voltage drop within the bilayer.) When $V < 1$, the solid and dashed lines are close to each other, which demonstrates that in this regime the charge reshuffling is dominated by the energy level shift. For larger V, the decrease (increase) of the electron density in the top (bottom) layer of the nonequilibrium system becomes slower and, after $V = 2$, the trend

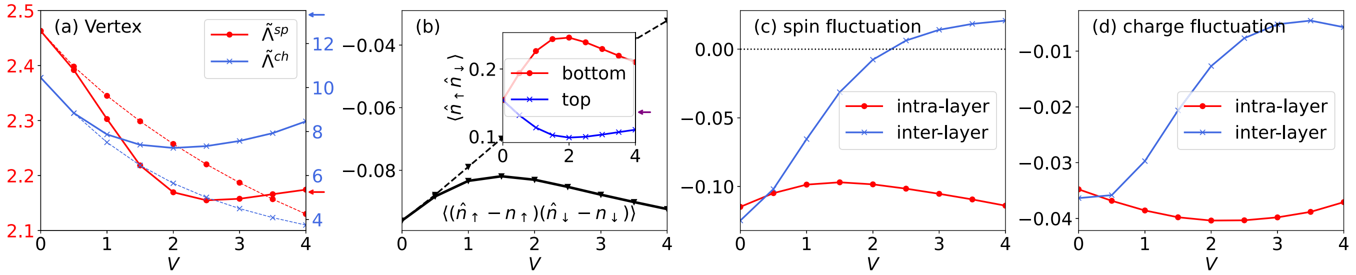

FIG. 6. Bias dependent two-particle quantities for the model depicted in Fig. 1(b) with parameters $W_1^\perp = 1$, $U = 4$, and $\beta = 4$. (a) Spin (red) and charge (blue) vertices. (b) Double occupancy fluctuation $\Delta D = \langle(\hat{n}_\uparrow - n_\uparrow)(\hat{n}_\downarrow - n_\downarrow)\rangle$, which is the same for both layers. Inset: Layer dependent $\langle \hat{n}_\uparrow \hat{n}_\downarrow \rangle$. In panels (a) and (b), the dashed lines show the results for the equilibrium doping model [see Fig. 1(c)], and the arrows on the right indicate the asymptotic values. (c, d) Nearest-neighbor intra- and interlayer spin and charge fluctuations, respectively.

is reversed. Physically, this happens because the overlap in the densities of states of the top and bottom layer is reduced with increasing V, so that the transfer of electrons between the two layers slows down. Note that in the limit of no hopping between the layers both layers will be half filled in our nonequilibrium setup.

In Fig. 5(b), we plot, in blue, the local spectral function $A(\omega) = -\mathrm{Im}G^r(\omega)/\pi$ of the top layer. (The spectral function for the bottom layer is mirrored at $\omega = 0$.) The occupied states $A^<(\omega) = \mathrm{Im}G^<(\omega)/(2\pi)$ of the upper layer are shown by the orange shading. The ratio between these two spectra defines the nonequilibrium distribution function $f_{\mathrm{neq}}(\omega) = A^<(\omega)/A(\omega)$, which is plotted as a red curve in the inset. This nonequilibrium distribution function deviates significantly from the Fermi function of the upper bath (right black line), and gives rise to the interesting nonequilibrium phenomena discussed below.

2. Two-particle properties

We now turn to the investigation of two-particle quantities, fixing $W_1^\perp = 1$ and $\beta = 4$ unless otherwise stated. Figure 6(a) plots the spin (red) and charge (blue) irreducible vertices as a function of the voltage bias. Again, the solid and dashed lines show the results for the nonequilibrium setup, Fig. 1(b), and the equilibrium system with shifted local energies, Fig. 1(c), respectively. Due to the electron-hole symmetry in the structure, the local vertices are identical on both layers. In contrast to the single layer case (see Appendix D), where an increase of V mainly leads to a heating effect, the vertices in the bilayer system exhibit a nonmonotonic behavior. Specifically, for small bias, both $\tilde{\Lambda}^{\mathrm{sp}}$ and $\tilde{\Lambda}^{\mathrm{ch}}$ decrease with increasing V. This effect mainly comes from the change in the filling of the layers, as the equilibrium model with shifted local energies predicts the qualitatively same behavior at small V. For $V \gtrsim 2$, both the spin and charge vertices start to grow. As discussed above, this is because for large V the layers are getting decoupled (reduced overlap in the local densities of states), so that the vertices are expected to approach the equilibrium values for decoupled layers with $\beta = 4$. These values, $\tilde{\Lambda}^{\mathrm{sp}} = 2.17$ and $\tilde{\Lambda}^{\mathrm{ch}} = 13.31$, are indicated by the arrows on the right.

In Fig. 6(b), we plot the bias dependent double occupancy fluctuation $\Delta D = \langle(\hat{n}_\uparrow - n_\uparrow)(\hat{n}_\downarrow - n_\downarrow)\rangle$ (same for both layers), where $n_\uparrow n_\downarrow$ is subtracted from $\langle \hat{n}_\uparrow \hat{n}_\downarrow \rangle$. The inset shows the layer dependent $\langle \hat{n}_\uparrow \hat{n}_\downarrow \rangle$, which is strongly influenced by the charge reshuffling. As expected in a repulsively interacting system, $\Delta D < 0$ due to the extra energy cost of double occupation. In the equilibrium system with shifted local energies [dashed black line in Fig. 6(b)], the correlation effects decrease with increasing charge polarization, so that ΔD approaches zero with increasing V. In the nonequilibrium setup, a similar trend is evident for small V, and hence can be attributed to the displacement of the onsite energies. As V increases, the system traverses a complex nonequilibrium regime but, for $V \gtrsim 2$, ΔD starts to approach the single layer equilibrium value (-0.114), due to the effective decoupling of the layers at very large V.

In Figs. 6(c) and 6(d), we plot the nearest-neighbor instantaneous spin and charge fluctuations, respectively. Also here, the term "fluctuation" refers to the fact that we subtract the expectation values from the operators, i.e., plot $\langle(\hat{X} - \langle\hat{X}\rangle)(\hat{Y} - \langle\hat{Y}\rangle)\rangle$, where $X, Y \in \hat{N}_i, \hat{S}_i^z$. This has no effect for the spin-spin correlations, since $\langle \hat{S}_i^z \rangle = 0$ in a paramagnetic state, but it shifts the charge-charge correlations by $N_i N_j$. The red (blue) curves are for intralayer (interlayer) correlations. The nonequilibrium results reveal that the intralayer fluctuations (red curves), both in the spin and charge channels, are rather insensitive to V, while the interlayer values (blue curves) react strongly to the voltage bias. Furthermore, the values of and changes in the spin fluctuations are roughly three times larger than the equilibrium values of and changes in the charge fluctuations, which is consistent with antiferromagnetically dominated short-range order in the structure. Remarkably, the interlayer spin fluctuations [solid blue line in Fig. 6(c)] change sign around $V = 2.25$, indicating a switch of the preferred interlayer spin alignment from AFM to ferromagnetic (FM). The TPSC+GG results (not shown) exhibit the same switching from antiferromagnetic to ferromagnetic spin correlations with increasing V. This switching cannot be explained by the electric field effect on the spin exchange coupling, which has been discussed in the case of Mott insulators [4,61], since the sign inversion of the exchange interaction requires $V \approx U$. Our observation is however consistent with Ref. [62], where the authors simulated the square lattice model subject to a short in-plane electric pulse using the FLEX+RPA method, and found a transient switch from antiferromagnetic to ferromagnetic correlations before relaxation.

To elucidate the spin dynamics, we perform calculations of the dynamical spin structure factor, also referred to as

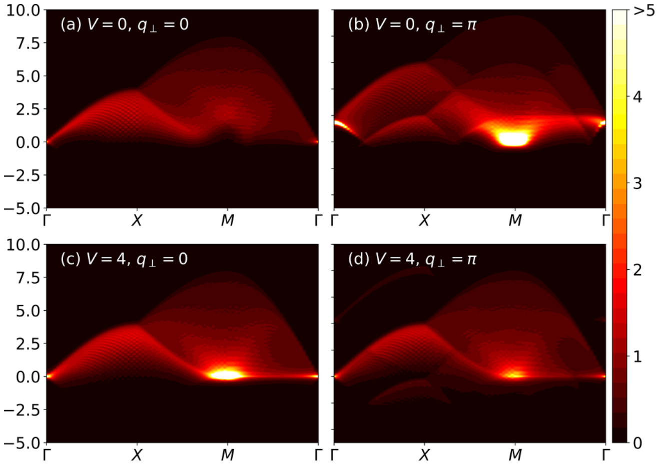

FIG. 7. Dynamical spin structure factor for $V=0$ (first row) and $V=4$ (second row), respectively. The left column shows the symmetric ($q_\perp=0$) channel and the right column shows the antisymmetric ($q_\perp=\pi$) channel. (Parameters: $W_1^\perp=1$, $U=4$, $\beta=4$.)

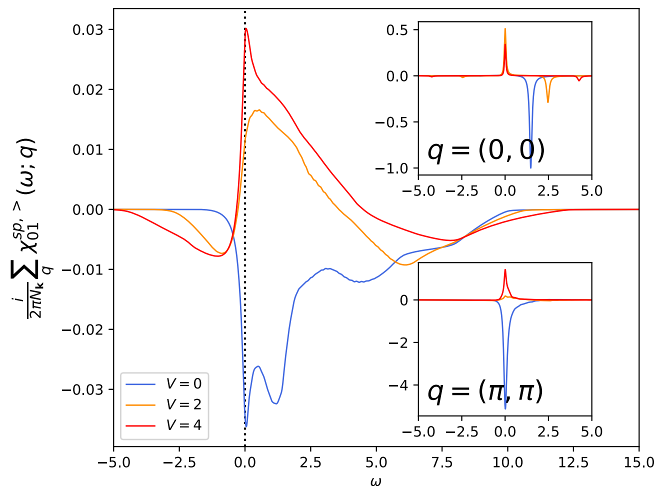

FIG. 8. Frequency-resolved and in-plane momentum averaged interlayer spin susceptibility (greater component) for different voltage biases. Insets: Contributions from $\mathbf{q}=(0,0)$ and (π,π). (Parameters: $W_1^\perp=1$, $U=4$, $\beta=4$.)

the (para)magnon dispersion. This quantity is defined as the the Fourier transform of the nonlocal spin-spin correlation function:

$$\sum_{\mathbf{T},T_\perp}\int\langle\hat{S}_i^z(t)\hat{S}^z_{i+\mathbf{T}+T_\perp}(t')\rangle e^{i[\mathbf{q}\cdot\mathbf{T}+q_\perp T_\perp+\omega(t-t')]}d(t-t') = \sum_{T_\perp} e^{iq_\perp T_\perp}\, i\chi^{\mathrm{sp},>}_{i,i+T_\perp}(\omega;\mathbf{q}), \qquad (33)$$

where $T_\perp$ takes the value 0 (1) for intralayer (interlayer) correlations. The corresponding $q_\perp$ values are zero and π, which represent the symmetric (bonding) and antisymmetric (antibonding) sectors. In Fig. 7, we plot the dynamical spin structure factor for $V=0$ (first row) and $V=4$ (second row), respectively. The left and right columns correspond to the symmetric ($q_\perp=0$) and antisymmetric ($q_\perp=\pi$) channels. In the equilibrium system, for $q_\perp=0$ [Fig. 7(a)], we see a linear dispersion around the Γ point ($\mathbf{q}=(0,0)$), while the antisymmetric channel [Fig. 7(b)] exhibits a large signal near the M point [$\mathbf{q}=(\pi,\pi)$]. These observations are qualitatively similar to the results for the bilayer Heisenberg model ($U\gg W$) obtained by QMC (see Fig. 1 in Ref. [63]). The most prominent effect of the bias $V=4$ [Figs. 7(c) and 7(d)] is a transfer of spectral weight from the antisymmetric to the symmetric channel around the M point, a result consistent with the observed switch from antiferromagnetic to ferromagnetic interlayer correlations. Given that the original TPSC method tends to overestimate correlation functions, it may be anticipated that these peaks will be smeared to some extent in more accurate calculations.

To gain further insights into the field-induced switching of the interlayer spin correlations shown in Fig. 6(c), we plot in Fig. 8 the momentum averaged interlayer dynamical spin structure factor $\frac{i}{2\pi N_{\mathbf{k}}}\sum_{\mathbf{q}}\chi_{01}^{\mathrm{sp},>}(\omega;\mathbf{q})$. This quantity represents the energy distribution of (in-plane momentum averaged) interlayer spin excitations, and its integral over ω yields the instantaneous interlayer spin correlation [see Eq. (32)]. In equilibrium (blue curve), the spectrum is negative and dominated by two low-energy peaks. The negative peak at $\omega=0$ predominantly originates from momentum $\mathbf{q}=(\pi,\pi)$, and thus forms a spin mode associated with both AFM interlayer spin alignment in the bilayer structure (negative sign) and AFM intralayer correlations, as can be seen from

$$\langle\hat{S}^z_{\mathbf{B}}(t)\hat{S}^z_{\mathbf{B}'+\mathbf{T}}(t')\rangle = \frac{1}{2\pi N_{\mathbf{k}}}\int d\omega\sum_{\mathbf{q}} i\chi^{\mathrm{sp},>}_{\mathbf{BB}'}(\omega;\mathbf{q})e^{-i[\mathbf{q}\cdot\mathbf{T}+\omega(t-t')]}. \qquad (34)$$

The above equation is a time nonlocal generalization of Eq. (32). The other prominent negative peak at $\omega\approx 1.16$ can be linked to in-plane momentum $\mathbf{q}=(0,0)$, and thus to an intraplane uniform but oscillating spin mode. The net effect of these correlations is a strengthening of interlayer singlet states within a unit cell. In the presence of a perpendicular electric field $V=4$, the dominant mode at $\omega=0$ and $\mathbf{q}=(\pi,\pi)$ changes its sign from negative to positive, thus contributing to an interlayer FM spin alignment (while the associated intralayer correlations remain AFM). Moreover, the negative weight of the mode at $\mathbf{q}=(0,0)$ is suppressed in the presence of the voltage bias. The result is a tendency to form interlayer spin triplet states within the unit cells.

Finally, we present in Fig. 9 the interlayer spin correlation $\langle\hat{S}_0^z\hat{S}_1^z\rangle$ as a function of interlayer coupling $W_1^\perp$ [Fig. 9(a)] and as a function of the bare Coulomb interaction U [Fig. 9(b)]. The blue and magenta curves in the insets correspond to the models depicted in Figs. 1(c) and 1(d), respectively. In Fig. 9(a), the effect of solely shifting the layer on-site energies (blue curves) or merely shifting the bath chemical potentials (magenta curves) is to make the interlayer spin correlation more negative. However, if both these changes are applied (red curves) the system exhibits ferromagnetic interlayer correlations in the hopping range $0<W_1^\perp\lesssim 1.75$, which is a completely nonlinear effect. For stronger $W_1^\perp$, antiferromagnetic interlayer correlations are recovered, since the electrons on different layers form a spin singlet. The interlayer

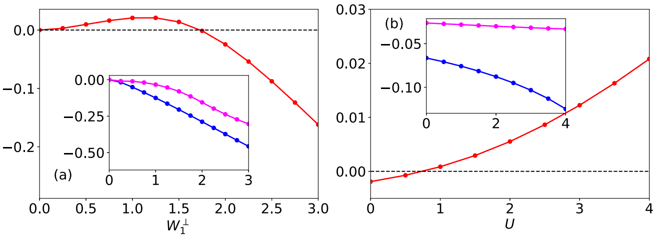

FIG. 9. Interlayer spin correlations for $V = 4$ as a function of (a) interlayer coupling $W_1^\perp$ (with $U = 4$, $\beta = 4$) and (b) Coulomb interaction U (with $W_1^\perp = 1$, $\beta = 4$). Insets: The blue and magenta curves show the results for the models illustrated in Figs. 1(c) and 1(d), respectively.

spin correlations will approach -0.5 in the large-$W_1^\perp$ limit. (For a pure singlet state, we have $\langle \hat{n}_{0\sigma}\hat{n}_{1\sigma}\rangle = 0$ and hence $\langle \hat{S}_0^z\hat{S}_1^z\rangle = \langle(\hat{n}_{0\uparrow} - \hat{n}_{0\downarrow})(\hat{n}_{1\uparrow} - \hat{n}_{1\downarrow})\rangle = -2\langle \hat{n}_{0\uparrow}\hat{n}_{1\downarrow}\rangle = -0.5$.) In Fig. 9(b), one can see that the interlayer spin correlations (in red) monotonically increase with increasing U, undergoing a sign switch from negative to positive around $U = 0.75$ for $V = 4$. In contrast, the equilibrium doping model (blue curve) shows an increase in AFM correlations with increasing U. This effect can be easily understood, since large U suppresses double occupations in each layer, thereby favoring the formation of a spin singlet state with antiparallel electrons in the different layers. Shifting the bath chemical potentials does not alter the position of the energy levels in the layers (in the wide-band approximation). The nonequilibrium effect results from the change in the occupation of the levels. The different qualitative behaviors of the interlayer spin correlations can be attributed to these nonequilibrium occupations. Our findings indicate that the model with a mere shift in the bath chemical potentials (magenta curve) exhibits a gradual increase in the AFM correlations. Both observations show that the switch from antiferromagnetic to ferromagnetic spin correlations is a nontrivial correlated-electron phenomenon driven by the external electric field.

IV. CONCLUSIONS

We developed nonequilibrium steady-state two-particle self-consistent schemes, and used them to study spin and charge correlations in a bilayer square lattice Hubbard model subject to a perpendicular static electric field. The TPSC method respects the Mermin-Wagner theorem, Pauli's exclusion principle, and various sum rules by self-consistently calculating vertex functions which are approximated as local in both space and time. From the local vertices, the nonlocal spatial correlations can then be obtained by solving the Schwinger-Dyson equation. Our steady-state formalism is based on a two-branch Schwinger-Keldysh contour, and employs Fourier transformations to frequency-momentum space. It thus gives access to the spectral properties of the system both in and out of equilibrium without numerical analytical continuation. In the applications, we mainly focused on the original TPSC method, which in contrast to TPSC+GG reproduces the pseudogap phenomenon related to short-ranged antiferromagnetic correlations. For the equilibrium bilayer square lattice Hubbard model, we calculated the evolution of the spectral function with increasing interlayer hopping, and illustrated the evolution from a system with antiferromagnetic pseudogap to a band insulator. We also demonstrated a good agreement of the calculated intra- and interlayer correlations with data from recent optical lattice experiments. This shows that the TPSC approach can reliably predict the nonlocal correlations in the considered parameter regime.

In the nonequilibrium calculations with perpendicular electric field, we observed that the system's behavior for small bias voltage is influenced by the charge reshuffling between the layers. With increasing bias or field strength, the system exhibits a nontrivial nonequilibrium behavior and finally approaches a state corresponding to decoupled equilibrium single layers in the limit of large V. The intralayer spin and charge correlations are not significantly affected by the electric field, while the interlayer correlations react strongly to the applied bias. More importantly, we found that the interlayer spin correlations switch from antiferromagnetic to ferromagnetic at some intermediate value of the perpendicular electric field when the intra- and interlayer couplings are comparable, which might have potential technological applications. Through comparison with the equilibrium effective doping model, we attribute this switching to the nonequilibrium population, which can be linked to the inversion of the spectrum for collective spin excitations.

ACKNOWLEDGMENT

The calculations were run on the Beo06 cluster at the University of Fribourg. We acknowledge support from Swiss National Science Foundation Grant No. 200021-196966 and thank O. Simard for helpful discussions.

APPENDIX A: FUNCTIONAL DERIVATIVE TECHNIQUE

We start from the partition function in the presence of an external source:

$$Z[\phi] = \mathrm{Tr}[T_\gamma(e^{-i\int_\gamma d\bar{z}\mathcal{H}(\bar{z})}\mathcal{S}[\phi])], \tag{A1}$$

where T_γ is the time ordering operator on the contour γ, which orders the operators from right to left with increasing contour time (with an additional minus sign for the exchange of two fermionic operators). In the above equation, a generic nondiagonal source field term,

$$\mathcal{S}[\phi] = e^{-i\int_\gamma d\bar{z}d\bar{z}'\sum_\sigma\sum_{ij}c^\dagger_{i\sigma}(\bar{z})\phi_{ij,\sigma\sigma'}(\bar{z},\bar{z}')c_{j\sigma'}(\bar{z}')}, \tag{A2}$$

is introduced for the purpose of deriving thermodynamically consistent quantities [25,27]. Physical quantities can be obtained by setting $\phi = 0$ in the end. To simplify the notation, we use a compressed notation $1 \equiv (i, z, \sigma)$, where i, z, and σ are site, contour time, and spin indices, respectively. With this, the source field term can be rewritten as

$$\mathcal{S}[\phi] = \exp\left\{-i\int d\bar{1}d\bar{2}c^\dagger(\bar{1})\phi(\bar{1},\bar{2})c(\bar{2})\right\}. \tag{A3}$$

The generating functional of the Green's function is defined as the logarithm of the partition function, $\mathcal{G}[\phi] = -\ln Z[\phi]$. Its first-order derivative with respect to ϕ yields the single-particle Green's function,

$$G(1,2;\phi) = -\frac{\delta \ln Z[\phi]}{\delta\phi(2,1)} = -i\langle T_\gamma c(1)c^\dagger(2)\rangle_\phi, \tag{A4}$$

where we introduced the expectation value

$$\langle T_\gamma\{\cdots\}\rangle_\phi = \frac{1}{Z[\phi]}\mathrm{Tr}\big[T_\gamma\big(e^{-i\int_\gamma d\bar{z}\mathcal{H}(\bar{z})}\mathcal{S}[\phi]\cdots\big)\big]. \tag{A5}$$

The derivative of $G(1,2;\phi)$ (corresponding to the second-order derivative of $\mathcal{G}[\phi]$) gives the two-particle exchange-correlation function

$$\begin{aligned} L(1,2,3,4;\phi) &= \frac{\delta G(1,3;\phi)}{\delta\phi(4,2)} \\ &= G(1,3;\phi)G(2,4;\phi) - G(1,2,3,4;\phi), \end{aligned} \tag{A6}$$

where

$$G(1,2,3,4;\phi) = (-i)^2\langle T_\gamma c(1)c(2)c^\dagger(4)c^\dagger(3)\rangle_\phi \tag{A7}$$

is the two-particle Green's function. The generalized four-point susceptibility is then defined as

$$\chi(1,2,3,4;\phi) = -iL(1,2,3,4;\phi). \tag{A8}$$

While the Green's function can be generated by the functional derivative of $\mathcal{G}[\phi]$, one can also introduce a generating functional of the vertex, which is the Legendre transform of $\mathcal{G}[\phi]$, i.e.,

$$\Gamma[G] = -\mathrm{Tr}(G*\phi) - \ln Z[\phi]. \tag{A9}$$

Here, we introduced the trace operator $\mathrm{Tr}A = \int d\bar{1}A(\bar{1},\bar{1})$ and the convolution $[A*B](1,2) = \int d\bar{3}A(1,\bar{3})B(\bar{3},2)$. The functional derivative of $\Gamma[G]$ with respect to G gives the source field:

$$\frac{\delta\Gamma[G]}{\delta G(2,1)} = -\phi(1,2). \tag{A10}$$

One usually separates the noninteracting contribution from $\Gamma[G]$, $\Gamma[G] = \Gamma^0[G] + \Phi[G]$, and thereby introduces the Luttinger-Ward functional $\Phi[G]$, which contains all the correlation contributions. $\Gamma^0[G]$ can be explicitly computed since the noninteracting action is Gaussian. Its explicit form reads $\Gamma^0[G] = -\mathrm{Tr}[(G^0)^{-1}*G - 1] + \mathrm{Tr}\ln(iG)$. As a result, we have

$$\Gamma[G] = -\mathrm{Tr}[(G^0)^{-1}*G-1] + \mathrm{Tr}\ln(iG) + \Phi[G]. \tag{A11}$$

$\Phi[G]$ is the generating functional of the two-particle irreducible vertices, and its first-order derivative gives the self-energy (one-particle irreducible vertex):

$$\Sigma(1,2) = \frac{\delta\Phi[G]}{\delta G(2,1)}. \tag{A12}$$

Applying the functional derivative with respect to G to Eq. (A11), one obtains the Dyson equation:

$$\frac{\delta\Gamma[G]}{\delta G(2,1^+)} = -[(G^0)^{-1}](1,2) + [G^{-1}](1,2) + \Sigma(1,2). \tag{A13}$$

Note that the term on the left-hand side is the source field, as seen from Eq. (A10), and thus vanishes for the physical model. The second-order derivative of $\Phi[G]$ with respect to G yields the two-particle (particle-hole) irreducible vertex:

$$\Lambda(1,2,3,4) = -\frac{\delta^2\Phi[G]}{\delta G(4,2)\delta G(3,1)} = -\frac{\delta\Sigma(1,3)}{\delta G(4,2)}. \tag{A14}$$

By taking the functional derivative of Eq. (A13) and using the identities (variables with overbars are integrated over)

$$\frac{\delta[G^{-1}](2,2')}{\delta G(1',1)} = -[G^{-1}](2,\bar{3})\frac{\delta G(\bar{3},\bar{4})}{\delta G(1',1)}[G^{-1}](\bar{4},2'), \tag{A15}$$

$$\frac{\delta^2 \ln Z[\phi]}{\delta\phi(\bar{6},\bar{5})\delta\phi(2,1)}\frac{\delta^2\Gamma[G]}{\delta G(4,3)\delta G(\bar{5},\bar{6})} = \delta(1-4)\delta(2-3), \tag{A16}$$

we finally arrive at the Bethe-Salpeter equation for the generalized susceptibility:

$$\begin{aligned} -i\chi(1,2,3,4) = &- iG(1,4)G(2,3) + iG(1,\bar{1})G(\bar{3},3) \\ &\times \Lambda(\bar{1},\bar{2},\bar{3},\bar{4})\chi(\bar{4},2,\bar{2},4). \end{aligned} \tag{A17}$$

For an alternative derivation of these results, see Ref. [46].

APPENDIX B: CONSISTENCY CONDITION FOR $[\Sigma^{(2)} * G^{(1)}]$

Here, we provide a brief proof of the nonequilibrium version of the consistency condition

$$[\Sigma^{(2)} * G^{(1)}](1,1^+) = iU(1)\big\langle\hat{n}_\sigma^{(1)}(1)\hat{n}_{-\sigma}^{(1)}(1)\big\rangle, \tag{B1}$$

where $\Sigma^{(2)}$ is calculated from Eq. (20) with $\alpha = 1$.

From the definition of $\Sigma^{(2)}$, we have

$$\begin{aligned} &[\Sigma^{(2)} * G^{(1)}](1,1^+) \\ &\quad = iU(1)[n(1)]^2 + i\frac{U(1)}{8}\frac{i}{2}\int d\bar{1}\chi^0(1,\bar{1}) \\ &\qquad \times [\Lambda^{\mathrm{ch}}(\bar{1})\chi^{\mathrm{ch}}(\bar{1},1) + 3\Lambda^{\mathrm{sp}}(\bar{1})\chi^{\mathrm{sp}}(\bar{1},1)], \end{aligned} \tag{B2}$$

where we have used $G(1,1^+) = in^{(1)}(1)$ and Eq. (18). With the relation $i\chi^0(1,1^+) = 2n^{(1)}(1)[1-n^{(1)}(1)]$, Eq. (17) and the spin and charge sum rules Eq. (11), after some algebra, one can prove Eq. (B1).

APPENDIX C: TPSC+GG SINGLE-LAYER SPECTRUM

Figure 10 plots the TPSC+GG results for the system with $W_1^\perp = 0$ in equilibrium, analogous to Fig. 2(a). In the first row, the local spectral function (left panel) and the momentum-resolved spectral function (middle panel) show no signs of an antiferromagnetic pseudogap, and also the Fermi surface estimated by $A(\mathbf{k};\omega = 0)$ (right panel) shows no clear suppression of the quasiparticles in the antinodal region. This indicates that as far as the pseudogap physics is concerned, the spectral properties of TPSC+GG are less reliable in the present parameter regime than those of standard TPSC. The second row of Fig. 10 further shows the evolution of the spectral function (red solid curve) in the

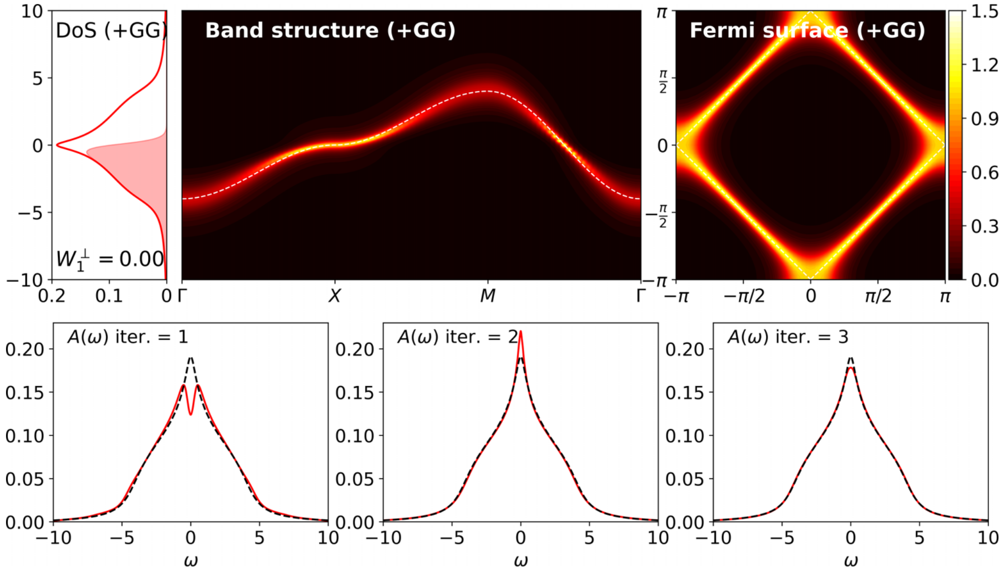

FIG. 10. Top panels: Spectral function, band structure, and Fermi surface obtained by TPSC+GG for $W_1^\perp = 0$ (single layer) in equilibrium at $\beta = 4$. These results can be compared to the corresponding TPSC data in Fig. 2(a). Bottom panels: Spectral functions for the first three iterations in the TPSC+GG calculation. Here, iter. = 1 corresponds to standard TPSC, while the dashed lines show the converged results.

first iterations of the TPSC+GG algorithm. The black dashed curve plots the converged TPSC+GG result for reference and "iter. = 1" corresponds to standard TPSC. One can see that the pseudogap disappears rapidly as the TPSC+GG iteration progresses. Inaccurate single-particle spectra are a common problem of self-consistent diagrammatic methods. In fact, the resummation of Feynman diagrams with the same topology in a self-consistent calculation can compromise relevant cancellations with other classes of diagrams [58] and result in poor spectra. However, despite this limitation, recent studies have shown that TPSC+GG provides a significantly improved description of the two-particle correlation functions [7,40].

APPENDIX D: BIAS INDUCED HEATING IN A SINGLE-LAYER LATTICE

In this Appendix, we study a single-layer square lattice under a perpendicular static electric field. The parameters are the same as in the bilayer case ($U = 4$, $\beta = 4$, and $\Gamma = 0.05$). In Fig. 11(a), we plot the spectral function for $V = 1$ (blue), the occupation (orange shading), as well as the corresponding nonequilibrium distribution function $f_{\text{neq}} = -\text{Im}G^</[2\text{Im}G^r]$ (orange line). By fitting $f_{\text{neq}}(\omega)$ with a Fermi function (red dashed line), one obtains the effective temperature $T_{\text{eff}} = 0.685$ of the nonequilibrium state. The good agreement between $f_{\text{neq}}(\omega)$ and the Fermi function indicates that the effect of a small bias is essentially a heating of the single-layer model ($T_{\text{eq}} = 0.25$). In Fig. 11(b), we plot the effective temperature as a function of voltage bias. Up to $V = 2$, the effective temperature description can capture the NESS characteristics of the system.

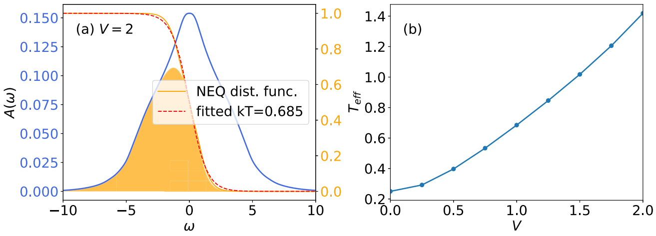

FIG. 11. (a) Local spectral function (in blue) and occupation (orange shaded area) for $V = 1$. The orange solid line shows the nonequilibrium distribution function and the red dashed line shows a fitted Fermi function. (b) Effective temperature as a function of voltage bias V.

To further validate the effective temperature description, we compared the vertices as well as local and nearest-neighbor correlations. In Table I, the first row shows the result for the nonequilibrium system with bias $V = 1$ and the second row shows the results for the equilibrium system with $T_{\text{eff}} = 0.685$. Again, one finds a remarkable agreement between the two systems. The relatively large (but still small in absolute values) error for $\tilde{\Lambda}^{\text{ch}}$ is due to its high sensitivity to the converged double occupation.

TABLE I. Comparison of vertices and correlation functions computed in the NESS for $V = 1.0$ and in the equilibrium system with $T = T_{\text{eff}} = 0.685$ (EQ).

	$\tilde{\Lambda}^{\text{sp}}$	$\tilde{\Lambda}^{\text{ch}}$	$\langle \hat{S}_0^z \hat{S}_0^z \rangle$	$\langle \hat{S}_0^z \hat{S}_1^z \rangle$	$\langle \hat{N}_0 \hat{N}_0 \rangle$	$\langle \hat{N}_0 \hat{N}_1 \rangle$
NESS	2.245	10.406	0.719	−0.098	0.281	−0.037
EQ	2.246	10.299	0.719	−0.097	0.281	−0.036

[1] B. Keimer, S. A. Kivelson, M. R. Norman, S. Uchida, and J. Zaanen, Nature (London) **518**, 179 (2015).

[2] D. Galanakis, E. Khatami, K. Mikelsons, A. Macridin, J. Moreno, D. A. Browne, and M. Jarrell, Philol. Trans. R. Soc. A **369**, 1670 (2011).

[3] H. Aoki, N. Tsuji, M. Eckstein, M. Kollar, T. Oka, and P. Werner, Rev. Mod. Phys. **86**, 779 (2014).

[4] Y. Murakami, D. Golež, M. Eckstein, and P. Werner, arXiv:2310.05201.

[5] J. P. F. LeBlanc, A. E. Antipov, F. Becca, I. W. Bulik, G. K.-L. Chan, C.-M. Chung, Y. Deng, M. Ferrero, T. M. Henderson, C. A. Jiménez-Hoyos, E. Kozik, X.-W. Liu, A. J. Millis, N. V. Prokof'ev, M. Qin, G. E. Scuseria, H. Shi, B. V. Svistunov, L. F. Tocchio, I. S. Tupitsyn *et al.* (Simons Collaboration on the Many-Electron Problem), Phys. Rev. X **5**, 041041 (2015).

[6] M. Qin, T. Schäfer, S. Andergassen, P. Corboz, and E. Gull, Annu. Rev. Condens. Matter Phys. **13**, 275 (2022).

[7] T. Schäfer, N. Wentzell, F. Šimkovic, Y.-Y. He, C. Hille, M. Klett, C. J. Eckhardt, B. Arzhang, V. Harkov, F. M. Le Régent, A. Kirsch, Y. Wang, A. J. Kim, E. Kozik, E. A. Stepanov, A. Kauch, S. Andergassen, P. Hansmann, D. Rohe, Y. M. Vilk *et al.*, Phys. Rev. X **11**, 011058 (2021).

[8] R. Orús, Nat. Rev. Phys. **1**, 538 (2019).

[9] W. Metzner and D. Vollhardt, Phys. Rev. Lett. **62**, 324 (1989).

[10] A. Georges and G. Kotliar, Phys. Rev. B **45**, 6479 (1992).

[11] A. Georges, G. Kotliar, W. Krauth, and M. J. Rozenberg, Rev. Mod. Phys. **68**, 13 (1996).

[12] G. Kotliar and D. Vollhardt, Phys. Today **57**, 53 (2004).

[13] E. Gull, A. J. Millis, A. I. Lichtenstein, A. N. Rubtsov, M. Troyer, and P. Werner, Rev. Mod. Phys. **83**, 349 (2011).

[14] P. Werner, A. Comanac, L. de' Medici, M. Troyer, and A. J. Millis, Phys. Rev. Lett. **97**, 076405 (2006).

[15] K. G. Wilson, Rev. Mod. Phys. **47**, 773 (1975).

[16] R. Bulla, T. A. Costi, and T. Pruschke, Rev. Mod. Phys. **80**, 395 (2008).

[17] T. A. Maier, M. Jarrell, T. Pruschke, and M. H. Hettler, Rev. Mod. Phys. **77**, 1027 (2005).

[18] G. Rohringer, H. Hafermann, A. Toschi, A. A. Katanin, A. E. Antipov, M. I. Katsnelson, A. I. Lichtenstein, A. N. Rubtsov, and K. Held, Rev. Mod. Phys. **90**, 025003 (2018).

[19] N. Tsuji, P. Barmettler, H. Aoki, and P. Werner, Phys. Rev. B **90**, 075117 (2014).

[20] M. Eckstein and P. Werner, Sci. Rep. **6**, 21235 (2016).

[21] N. Bittner, D. Golež, M. Eckstein, and P. Werner, Phys. Rev. B **101**, 085127 (2020).

[22] V. Janiš and P. Augustinský, Phys. Rev. B **77**, 085106 (2008).

[23] V. Janiš, A. Kauch, and V. Pokorný, Phys. Rev. B **95**, 045108 (2017). V. Janiš, V. Pokorný, and A. Kauch, *ibid.* **95**, 165113 (2017).

[24] P. Zalom, V. Pokorný, and V. Janiš, Phys. B: Condens. Matter **536**, 704 (2018).

[25] Y. Vilk and A.-M. Tremblay, J. Phys. I (Paris) **7**, 1309 (1997).

[26] A.-M. S. Tremblay, in *Strongly Correlated Systems: Theoretical Methods*, edited by A. Avella and F. Mancini (Springer-Verlag, Berlin, 2012), pp. 409–453.

[27] L. P. Kadanoff and G. A. Baym, *Quantum Statistical Mechanics* (Benjamin, New York, 1962).

[28] H. Bruus and K. Flensberg, *Many-Body Quantum Theory in Condensed Matter Physics: An Introduction* (Oxford University Press, New York, 2004).

[29] K. Held, A. A. Katanin, and A. Toschi, Prog. Theor. Phys. Suppl. **176**, 117 (2008).

[30] A. N. Rubtsov, M. I. Katsnelson, and A. I. Lichtenstein, Phys. Rev. B **77**, 033101 (2008).

[31] Y. M. Vilk, L. Chen, and A.-M. S. Tremblay, Phys. Rev. B **49**, 13267 (1994).

[32] B. Davoudi and A.-M. S. Tremblay, Phys. Rev. B **76**, 085115 (2007).

[33] D. Lessnich, C. Gauvin-Ndiaye, R. Valentí, and A. M. S. Tremblay, Phys. Rev. B **109**, 075143 (2024).

[34] H. Miyahara, R. Arita, and H. Ikeda, Phys. Rev. B **87**, 045113 (2013).

[35] K. Zantout, S. Backes, and R. Valentí, Ann. Phys. (Leipzig) **533**, 2000399 (2021).

[36] C. Gauvin-Ndiaye, J. Leblanc, S. Marin, N. Martin, D. Lessnich, and A. M. S. Tremblay, arXiv:2308.14091.

[37] C. Gauvin-Ndiaye, C. Lahaie, Y. M. Vilk, and A.-M. S. Tremblay, Phys. Rev. B **108**, 075144 (2023).

[38] N. Martin, C. Gauvin-Ndiaye, and A.-M. S. Tremblay, Phys. Rev. B **107**, 075158 (2023).

[39] K. Zantout, S. Backes, A. Razpopov, D. Lessnich, and R. Valentí, Phys. Rev. B **107**, 235101 (2023).

[40] O. Simard and P. Werner, Phys. Rev. B **107**, 245137 (2023).

[41] J. Yan and V. Janiš, Phys. Rev. B **105**, 085122 (2022).

[42] O. Simard and P. Werner, Phys. Rev. B **106**, L241110 (2022).

[43] S. Karakuzu, S. Johnston, and T. A. Maier, Phys. Rev. B **104**, 245109 (2021).

[44] C. Yue, H. Aoki, and P. Werner, Phys. Rev. B **106**, L180506 (2022).

[45] Y. Zeng, V. Crépel, and A. J. Millis, arXiv:2311.04074.

[46] G. Stefanucci and R. Van Leeuwen, *Nonequilibrium Many-Body Theory of Quantum Systems: A Modern Introduction* (Cambridge University Press, New York, 2013).

[47] H. Haug, A.-P. Jauho, and M. Cardona, *Quantum Kinetics in Transport and Optics of Semiconductors* (Springer, New York, 2008), Vol. 2.

[48] $2 \to 1^-$ leads to the same results, since $\chi^{\mathrm{sp/ch}}(1, 1^+) = \chi^{\mathrm{sp/ch}}(1, 1^-)$.

[49] G. Baym and L. P. Kadanoff, Phys. Rev. **124**, 287 (1961).

[50] Y. Vilk, L. Chen, and A.-M. Tremblay, Physica C **235**, 2235 (1994).

[51] S. Allen, A. M. S. Tremblay, and Y. M. Vilk, in *Theoretical Methods for Strongly Correlated Electrons*, edited by D. Sénéchal, A.-M. Tremblay, and C. Bourbonnais (Springer, New York, 2004), pp. 341–355.

[52] J. Yan and P. Werner, Phys. Rev. B **108**, 125143 (2023).

[53] J. Yan and Y. Ke, Phys. Rev. B **94**, 045424 (2016).

[54] S. Datta, *Quantum Transport: Atom to Transistor* (Cambridge University Press, New York, 2005).

[55] M. Klett, N. Wentzell, T. Schäfer, F. Simkovic, O. Parcollet, S. Andergassen, and P. Hansmann, Phys. Rev. Res. **2**, 033476 (2020).

[56] S. Brener, H. Hafermann, A. N. Rubtsov, M. I. Katsnelson, and A. I. Lichtenstein, Phys. Rev. B **77**, 195105 (2008).

[57] M. Golor, T. Reckling, L. Classen, M. M. Scherer, and S. Wessel, Phys. Rev. B **90**, 195131 (2014).

[58] J. Gukelberger, L. Huang, and P. Werner, Phys. Rev. B **91**, 235114 (2015).

[59] M. Eckstein, M. Kollar, and P. Werner, Phys. Rev. B **81**, 115131 (2010).

[60] M. Gall, N. Wurz, J. Samland, C. F. Chan, and M. Köhl, Nature (London) **589**, 40 (2021).

[61] S. Trotzky, P. Cheinet, S. Fölling, M. Feld, U. Schnorrberger, A. M. Rey, A. Polkovnikov, E. A. Demler, M. D. Lukin, and I. Bloch, Science **319**, 295 (2008).

[62] N. Dasari and M. Eckstein, Phys. Rev. B **100**, 121114(R) (2019).

[63] M. Lohöfer, T. Coletta, D. G. Joshi, F. F. Assaad, M. Vojta, S. Wessel, and F. Mila, Phys. Rev. B **92**, 245137 (2015).